



# Correlation between catalytic activity and catalytic surface area of a Pt/Al<sub>2</sub>O<sub>3</sub> DOC: An experimental and microkinetic modeling study



Denise Chan<sup>a</sup>, Steffen Tischer<sup>b</sup>, Jasmin Heck<sup>a</sup>, Claudia Diehm<sup>b</sup>, Olaf Deutschmann<sup>a,b,\*</sup>

<sup>a</sup> Institute for Chemical Technology and Polymer Chemistry, Karlsruhe Institute of Technology (KIT), 76128 Karlsruhe, Germany

<sup>b</sup> Institute for Catalysis Research and Technology, Karlsruhe Institute of Technology (KIT), 76128 Karlsruhe, Germany

## ARTICLE INFO

### Article history:

Received 15 November 2013

Received in revised form 27 February 2014

Accepted 7 March 2014

Available online 15 March 2014

### Keywords:

DOC aging

Pt dispersion

CO oxidation

Structure sensitivity

Microkinetic model

## ABSTRACT

The readjustment of kinetic parameters in models of automotive catalytic converters due to catalyst aging calls for a better understanding of the correlation between model parameters and easily accessible quantitative catalyst properties. It is shown by means of CO light-off and CO chemisorption measurements that the catalytic activity of a commercial Pt/Al<sub>2</sub>O<sub>3</sub> diesel oxidation catalyst can be successfully correlated to the catalytic surface area. This correlation exhibits the same trend for all investigated aging temperatures, aging times and lean aging atmospheres. However, no distinct correlation between catalytic activity and catalytic surface area is found for aging treatment in N<sub>2</sub>. The mechanism of noble metal sintering seems to depend on the oxygen content of the aging atmosphere and aging in N<sub>2</sub> leads to a particle size distribution which is more beneficial to the catalyst activity, as compared to the particle sizes arising from lean aging conditions. This observation also implies that CO oxidation over platinum is structure sensitive. Furthermore, a refined microkinetic model for the platinum catalyzed oxidation of CO is developed which comprises two different paths for CO<sub>2</sub> formation. The experimentally found correlation between catalytic activity and catalytic active surface area is successfully used for simulation of the activity change caused by lean hydrothermal aging. Spatially resolved gas phase concentration profiles of CO and CO<sub>2</sub> during CO oxidation at full conversion are measured for further validation of the model.

© 2014 Elsevier B.V. All rights reserved.

## 1. Introduction

Mostly driven by environmental and health concerns, increasingly stringent legislative regulations of exhaust gas emissions pose a challenge to exhaust gas after-treatment systems. Due to the rising demand of mobility, the increasing number of vehicles worldwide also requires more fuel efficient engines in order to confine greenhouse gas emissions, such as CO<sub>2</sub>. One possibility to meet these requirements is the usage of lean-burn engines [1–6]. However, the abatement of nitrogen oxides (NO<sub>x</sub>) and particulate matter emissions is challenging and implies a systematic combination of several abatement units for diesel applications: diesel oxidation catalyst (DOC), diesel particulate filter (DPF), DeNO<sub>x</sub> systems (SCR, NSC) [7].

The present work focuses on the DOC which is the first catalytic converter unit downstream of the engine. Its task is to promote the oxidation of unburned hydrocarbons and CO on the one hand, and to provide a sufficiently high NO<sub>2</sub>/NO<sub>x</sub>-ratio for the subsequent catalysts (NSC, SCR, CRT-DPF) on the other hand. Therefore, the activity of the DOC has a strong influence on the whole after-treatment system.

In order to ensure optimal operation conditions, the current, aging dependent catalyst state during vehicle operation has to be considered when developing operation strategies and engine control concepts. Development and optimization of such concepts and the design of exhaust systems are complex processes which require a simulation-supported approach to limit costs and development time [8]. By now, the adjustment of simulation models to aged catalyst states demands comprehensive experimental investigations and model recalibration.

Based on a close-to-reality model diesel oxidation catalyst, it has been shown in a previous study that a successful correlation of reaction kinetic parameters with characteristic variables of the catalyst substantially simplifies the recalibration of an existing model in the case of activity change [9,10]. For structure insensitive

\* Corresponding author at: Institute for Chemical Technology and Polymer Chemistry, Karlsruhe Institute of Technology (KIT), 76128 Karlsruhe, Germany. Tel.: +49 721 608 43064; fax: +49 721 608 44805.

E-mail address: [deutschmann@kit.edu](mailto:deutschmann@kit.edu) (O. Deutschmann).

**Table 1**  
Lean model exhaust gas compositions for aging treatment.

Component	Lean, NO <sub>x</sub> -free	Lean, NO <sub>x</sub> -containing
NO [vol.-ppm]	0	1000
NO <sub>2</sub> [vol.-ppm]	0	70
C <sub>3</sub> H <sub>6</sub> [vol.-ppm]	100	100
O <sub>2</sub> [vol.%]	12	12
CO [vol.%]	0.04	0.04
CO <sub>2</sub> [vol.%]	7	7
H <sub>2</sub> O [vol.%]	10	10
N <sub>2</sub>	Balance	Balance

reactions, the catalytic surface area served as a model parameter for the consideration of varying noble metal loading. Further adaptations of kinetic parameters were not necessary. However, concerning activity change caused by hydrothermal aging, the correlation was only established for the variation of aging temperature while the aging time as well as the aging atmosphere remained constant.

The aim of the present work is to create a broad experimental foundation for the existing correlation by comprehensive variation within the parameter matrix. For this purpose, a commercial Pt/Al<sub>2</sub>O<sub>3</sub> DOC was hydrothermally aged under a broad range of conditions. Thereby, the aging temperature and the aging time as well as the aging atmosphere were varied. Subsequently, the platinum dispersion was determined and CO light-off experiments, serving as a measure for the catalytic activity, were performed.

Furthermore, a refined microkinetic model for the platinum catalyzed oxidation of CO in a DOC was developed which accounts for the found correlation between catalytic activity and catalytic surface area.

## 2. Experimental

### 2.1. Catalyst samples and aging conditions

For this study, a commercial diesel oxidation catalyst provided by Umicore AG & Co. KG was used. The washcoat comprising of 147 g/ft<sup>3</sup> Pt/Al<sub>2</sub>O<sub>3</sub> is supported by a honeycomb cordierite monolith with a cell density of 400 cps.

The catalytic surface area and the catalytic activity were determined subsequent to various aging treatments. Thereby, the aging temperature and the aging time as well as the aging atmosphere (N<sub>2</sub>, air + 10 vol.% H<sub>2</sub>O, lean NO<sub>x</sub>-free model exhaust gas, lean NO<sub>x</sub>-containing model exhaust gas) were varied (Fig. 1). The composition of the lean model exhaust gas is depicted in Table 1. Aging was performed under a flow rate of 2.5 L/min at standard ambient temperature and pressure (SATP, 298 K, 1013 hPa). One sample was used for each pair of aging temperature and atmosphere. In order to ensure the comparability of the samples employed for the study, a sample screening had been performed prior to aging treatment and measurements. For this purpose, 36 cores (19 mm diameter, 27 mm length) were drilled out from 3 cordierite monolith blocks and degreened for 1 h at 550 °C in 1 vol.% CO, 7 vol.% CO<sub>2</sub>, 10 vol.% H<sub>2</sub>O, 12 vol.% O<sub>2</sub>, and N<sub>2</sub> balance with a flow rate of 5 L/min, corresponding to a gas hourly space velocity (GHSV) of 40,000 h<sup>-1</sup> at SATP. Subsequently, the CO light-off temperature of each sample was determined using a heating rate of 3 K/min and the same gas mixture and flow rate as for degreening. By this means, 16 samples with similar activity could be identified and were chosen for the establishment of an aging correlation.

### 2.2. Experimental set-up

The catalytic surface area, which corresponds to the Pt dispersion, was determined by CO chemisorption measurements while the light-off of the CO oxidation reaction served as a measure for

the relative catalytic activity. The aging treatments as well as the CO light-off experiments and dispersion measurements were carried out within the same experimental setup (Fig. 2). The core samples were inserted in a quartz tube flow reactor (21 mm inner diameter) using ceramic fiber paper to eliminate gas bypass. Mass flow controllers (Bronkhorst) were used for gas dosing; a Fourier transform infrared (FTIR) spectrometer (MKS Multigas 2030) was applied for online gas analysis. The reactor was heated by an electrical furnace and the temperature was monitored by two K-type thermocouples placed at the reactor inlet and outlet, respectively.

### 2.3. Dispersion measurements

The Pt dispersion was measured by continuous-flow CO TPD with a flow rate of 1 L/min at SATP. To insure reproducible conditions, the catalyst was pretreated with 5 vol.% H<sub>2</sub>, diluted in N<sub>2</sub> for 30 min at 673 K before every measurement. Subsequently, the reactor was cooled down to room temperature under N<sub>2</sub> flow. After saturation of the catalyst with 5 vol.% CO in N<sub>2</sub>, the reactor was purged for 30 min with N<sub>2</sub> in order to remove physisorbed CO. TPD was performed with a linear heating rate of 30 K/min from room temperature to the maximum temperature of 823 K under continuous N<sub>2</sub> flow. A high heating rate was chosen to achieve sharp desorption peaks and therewith a good signal/noise ratio. During TPD, the gas phase concentrations of CO and CO<sub>2</sub> at the reactor outlet were monitored by FTIR. For the determination of the baseline, empty pipe measurements were performed applying the same procedure. Every measurement was validated by a second run.

Although the average CO:Pt adsorption stoichiometry generally varies from 1:1 to 2:1 since CO chemisorbs in various forms, depending on temperature and pressure as well as the type of adsorption sites, for calculation of the noble metal dispersion it is commonly supposed to be 1:1 [11]. Owing to better comparability, the same assumption was made in this work. Furthermore, it was assumed that both C-species detected during TPD, i.e., CO and CO<sub>2</sub>, originated in adsorbed CO [12].

### 2.4. CO light-off measurements

CO light-off measurements were performed with 1 vol.% CO, 7 vol.% CO<sub>2</sub>, 10 vol.% H<sub>2</sub>O, 12 vol.% O<sub>2</sub>, N<sub>2</sub> balance and a flow rate of 5 L/min (40,000 h<sup>-1</sup> GHSV) at SATP. The temperature at which 50% of the CO is oxidized (hereafter referred to as CO light-off temperature or T<sub>50</sub>), was determined and served as a measure for the catalytic activity. A small heating rate of 3 K/min was chosen for high precision. Every measurement could be reproduced by a second run.

### 2.5. Axial concentration profile

Spatially resolved gas phase concentration profiles of CO and CO<sub>2</sub> during CO oxidation at full conversion were measured for the catalyst sample aged for 96 h at 650 °C in lean NO<sub>x</sub>-containing model exhaust gas. For this experiment, the same gas mixture and the same flow rate were chosen as for CO light-off measurements. The temperature at the reactor inlet was 508 K.

The experimental set-up was similar to the one used for catalyst aging, dispersion measurements and CO light-off experiments. For in situ measurement of the axial concentration profiles, a deactivated, fused silica capillary with an outer diameter of 170 μm was placed inside the central channel of the monolithic sample. A constant gas flow of 2 mL/min was sucked through the capillary by a pump. The axial sampling position within the channel was controlled by a motorized linear stage. A detailed description of the applied suction probe technique can be found elsewhere [13].

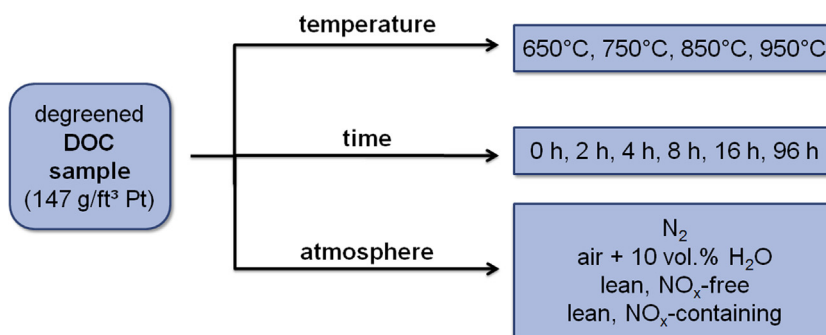


Fig. 1. Aging conditions.

### 3. Numerical model

#### 3.1. Reactor models

Modeling was performed for one representative channel of the monolithic sample. This approach is justified for the simulation of the experiments in this work because no radial gradients are expected at the catalyst inlet. Cylindrical symmetry is assumed for the washcoated channels.

##### 3.1.1. CO light-off simulation

For modeling of the CO light-off experiments, the DETCHEM<sup>CSTR</sup> code was applied which allows for fully transient simulation based on the model of the continuously stirred tank reactor [14]. A cascade of 100 CSTRs was used for the numerical description of a plug flow reactor. The inlet conditions of the  $n$ th CSTR within the cascade are given by the outlet conditions of the  $(n - 1)$ th CSTR:

Continuity equation

$$\frac{dn_i}{dt} = \dot{n}_{i,n-1} - \dot{n}_{i,n} + A_{cat}\dot{s}_i \quad (1)$$

Energy continuity

$$\frac{dH}{dt} \sum_{i=1}^{N_g} \dot{n}_{i,n-1} h(T_{n-1}) - \sum_{i=1}^{N_g} \dot{n}_{i,n} h(T_n) + k_w A_{geo} (T_w - T) \quad (2)$$

The definition of all variables is depicted in Tables 2 and 3.

##### 3.1.2. Simulation of spatially resolved concentration profiles

For simulation of steady-state conditions, a more detailed flow field model was applied. The DETCHEM<sup>CHANNEL</sup> code computes the steady-state two-dimensional flow through a cylindrical channel using the boundary-layer approximation. The boundary-layer approach provides accurate results at much lower computational cost than the full Navier–Stokes model as long as the Reynolds

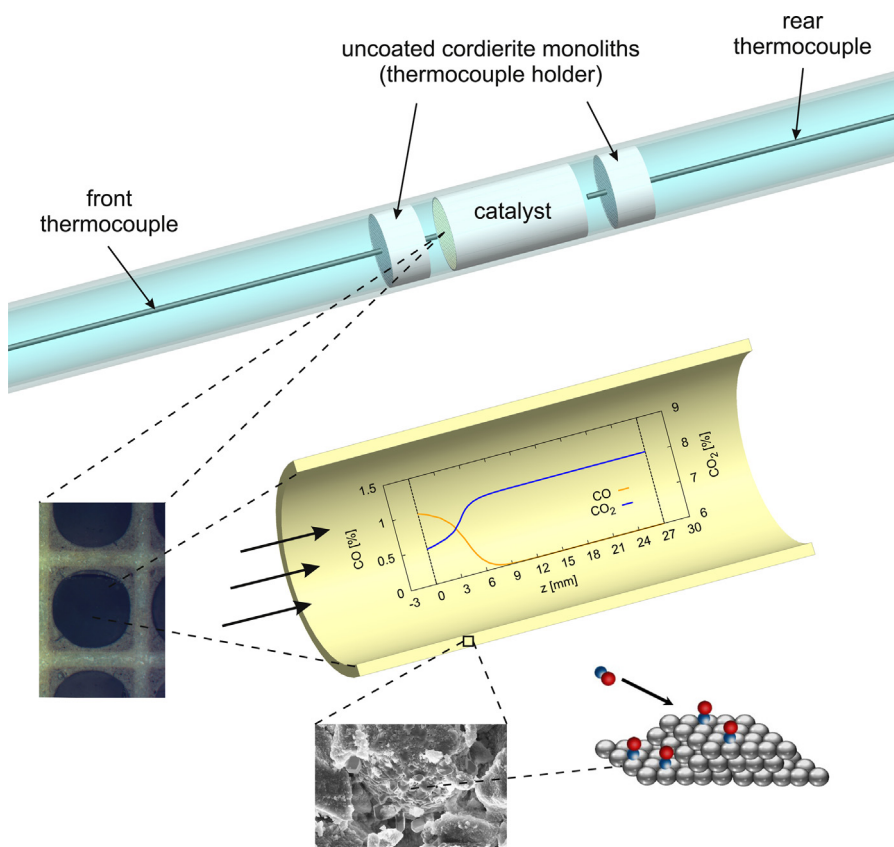


Fig. 2. Sketch of the experimental setup and the catalyst structure.

**Table 2**  
Notation, Latin letters.

Notation		Unit
$A_{\text{cat}}$	Catalytically active surface area	$\text{m}^2$
$A_{\text{geo}}$	Geometrical surface area	$\text{m}^2$
$A_k$	Pre-exponential factor	$\text{mol}, \text{cm}, \text{s}$
$c_i$	Concentration of species $i$	$\text{mol m}^{-3}, \text{mol m}^{-3}$
$D$	Dispersion	
$\bar{D}_i$	Effective diffusion coefficient	$\text{m}^2 \text{s}^{-2}$
$E_{\text{ak}}$	Activation energy	$\text{kJ mol}^{-1}$
$F_{\text{cat/geo}}$	Ratio of catalytic and geometrical surface area	
$h_i$	Species enthalpy	$\text{J kg}^{-1}$
$j_{i,r}$	Radial diffusion flux	$\text{mol m}^{-2} \text{s}^{-1}$
$k_{\text{eff},i}$	Effective rate coefficient	$\text{s}^{-1}$
$k_{\text{fk}}$	Forward reaction rate coefficient	Various
$k_{\text{rk}}$	Reverse reaction rate coefficient	Various
$k_w$	Heat transfer coefficient	$\text{J s}^{-1} \text{m}^{-2} \text{K}^{-1}$
$K_s$	Number of surface reactions	
$L$	Wash coat thickness	$\text{m}$
$h_i$	Species enthalpy	$\text{J kg}^{-1}$
$m_{\text{cat}}$	Catalyst mass	$\text{kg}$
$M_{\text{cat}}$	Catalyst molar mass	$\text{kg mol}^{-1}$
$M_i$	Species molecular weight	$\text{kg mol}^{-1}$
$n_i$	Mole fraction of species $i$	
$N_g$	Number of gas phase species	
$N_s$	Number of surface species	
$p$	Pressure	$\text{Pa}$
$q_r$	Heat flux density	$\text{J s}^{-1} \text{m}^{-2}$
$r$	Channel radius	$\text{m}$
$R$	Universal gas constant	$\text{J mol}^{-1} \text{K}^{-1}$
$\dot{s}_i$	Surface reaction rate	$\text{mol m}^{-2} \text{s}^{-1}$
$t$	Time	$\text{s}$
$T$	Temperature	$\text{K}$
$T_w$	Wall temperature	$\text{K}$
$u$	Axial velocity	$\text{ms}^{-1}$
$v$	Radial velocity	$\text{m s}^{-1}$
$Y_i$	Mass fraction of species $i$	
$z$	Axial coordinate	$\text{m}$

number is sufficiently high, e.g., the diffusive transport along the axial direction is negligible compared to the convective flow [15]. This requirement is satisfied by all cases studied within the present work. The boundary-layer approach yields following governing equations [15–17]:

Continuity equation

$$\frac{\partial(\rho u)}{\partial z} + \frac{1}{r} \frac{\partial(r \rho v)}{\partial r} = 0 \quad (3)$$

Axial momentum

$$\rho u \frac{\partial u}{\partial z} + \rho v \frac{\partial u}{\partial r} = -\frac{\partial p}{\partial z} + \frac{1}{r} \frac{\partial}{\partial r} \left( \mu r \frac{\partial u}{\partial r} \right) \quad (4)$$

**Table 3**  
Notation, Greek letters.

Notation		Unit
$\beta_k$	Parameter for temperature dependency of $A_k$	
$\Gamma$	Surface site density	$\text{mol m}^{-2}$
$\varepsilon_p$	Porosity	
$\varepsilon_{ik}$	Parameter for coverage dependent activation energy	$\text{kJ mol}^{-1}$
$\eta$	Effectiveness factor	
$\Theta_i$	Surface coverage with species $i$	
$\lambda$	Thermal conductivity	$\text{J m}^{-1} \text{s}^{-1} \text{K}^{-1}$
$\mu$	Viscosity	$\text{kg m}^{-1} \text{s}^{-1}$
$\mu_{ik}$	Parameter for coverage dependent reaction order	
$\nu_{ik}$	Stoichiometric coefficient	
$\rho$	Density	$\text{kg m}^{-3}$
$\sigma_i$	Number of occupied surface sites	
$\tau$	Tortuosity	
$\phi$	Thiele modulus	
$\dot{\omega}_i$	Gas phase reaction rate	$\text{mol m}^{-3} \text{s}^{-1}$
$i$	Species number	
$k$	Reaction number	

Radial momentum

$$\frac{\partial p}{\partial r} = 0 \quad (5)$$

Species continuity

$$\rho u \frac{\partial Y_i}{\partial z} + \rho v \frac{\partial Y_i}{\partial r} = -\frac{1}{r} \frac{\partial(r j_{i,r})}{\partial r} \quad (6)$$

Energy continuity

$$\rho u \frac{\partial h}{\partial z} + \rho v \frac{\partial h}{\partial r} = u \frac{\partial p}{\partial z} - \frac{1}{r} \frac{\partial(r q_r)}{\partial r} \quad (7)$$

With  $j_{i,r}$  being the diffusion mass flux at the interface of free fluid flow and washcoat:

$$j_{i,r} = -\eta F_{\text{cat/geo}} M_i \dot{s}_i \quad (8)$$

The application of the effectiveness factor  $\eta$  accounts for the transport limitation by pore diffusion within the porous washcoat. This zero-dimensional diffusion model is based on the analytical solution of a reaction-diffusion equation for a single representative species expressed in terms of the Thiele modulus [18–21]. In the present work, CO is regarded as the effectiveness factor species. A detailed description and evaluation of the effectiveness factor approach can be found elsewhere [22].

The model parameter  $F_{\text{cat/geo}}$  denotes the ratio of the catalytic surface area to the geometrical area of the catalyst, i.e., in the present case, the ratio of the noble metal area accessible for catalytic reactions to the geometrical area of the cylindrical walls of the monolith channel. It is directly proportional to the noble metal dispersion which can be experimentally determined by CO chemisorption.

$$F_{\text{cat/geo}} = \frac{A_{\text{cat}}}{A_{\text{geo}}} = D \frac{m_{\text{cat}}}{M_{\text{cat}} \Gamma_{\text{cat}} A_{\text{geo}}} \quad (9)$$

### 3.1.3. Mass transport limitations in washcoats

The factor  $\eta$  in Eq. (8) accounts for the transport limitation by pore diffusion within the porous washcoat. It can be calculated by solving a reaction-diffusion equation within the porous layer

$$\frac{\partial}{\partial r} \left( -\frac{\varepsilon_p}{\tau} \bar{D}_i \frac{\partial c_i}{\partial r} \right) = \frac{F_{\text{cat/geo}}}{L} \dot{s}_i \quad (10)$$

Here  $\bar{D}_i$  denotes the mixture averaged diffusion coefficient, which includes molecular as well as Knudsen diffusion;  $\varepsilon_p$  is the porosity,  $\tau$  the tortuosity and  $L$  the washcoat thickness. For the present calculations, values of 0.5 and 3 for the porosity and the tortuosity were applied, respectively. The mean pore diameter was assumed to be 100 nm and the thickness of the washcoat layer was determined to be 0.1 mm by light microscopy.

However, since the solution of the reaction-diffusion equation is numerically expensive, a zero-dimensional diffusion model based on the analytical solution of the reaction-diffusion equation for a single representative species expressed in terms of the Thiele modulus  $\Phi$  is preferably used [18–21].

$$\Phi = L \sqrt{\frac{k_{\text{eff},i}}{(\varepsilon_p/\tau) \bar{D}_i}} \quad (11)$$

$k_{\text{eff},i}$  is the effective rate coefficient for an assumed first-order reaction of species  $i$ , for which throughout this paper CO is chosen. Then the effectiveness factor can be expressed as

$$\eta = \frac{\tanh \Phi}{\Phi} \quad (12)$$

A detailed description and evaluation of the effectiveness factor approach can be found elsewhere [22].



### 3.2. Surface chemistry model

Since gas phase reactions are not occurring under the experimental conditions of the present work, surface reactions are regarded exclusively in the elementary-step based reaction mechanism. The chemical source term due to surface reactions in Eqs. (1) and (8) can be written as [16,23]:

$$\dot{S}_i = \sum_{k=1}^{K_s} v_{ik} k_{fk} \prod_{j=1}^{N_g+N_s} c_j^{v_j^k} \quad (13)$$

The rate coefficient of the surface reactions  $k_{fk}$  is described by a modified Arrhenius expression:

$$k_{fk} = A_k T^{\beta_k} \exp \left[ -\frac{E_{a_k}}{RT} \right] \prod_{i=1}^{N_s} \exp \left[ \frac{\varepsilon_{ik} \Theta_i}{RT} \right] \quad (14)$$

The additional model parameter  $\varepsilon_{ik}$  accounts for the coverage dependency of the activation energy.

For adsorption reactions, the rate coefficient is described in terms of a sticking coefficient:

$$k_{fk}^{\text{ads}} = \frac{S_i^0}{F^\tau} \sqrt{\frac{RT}{2\pi M_i}} \quad (15)$$

### 3.3. Thermodynamic consistency

The proposed reaction mechanism consists of pairs of reversible reactions. The equilibrium condition between a forward (f) and its reverse reaction (r) leads to the equation

$$\frac{k_{fk}(T)}{k_{rk}(T)} = \exp \left( -\frac{\Delta_{Rk}G(T)}{RT} \right) \prod_{i=1}^{N_g+N_s} c_{i,0}^{v_{ik}} \quad (16)$$

where  $\Delta_{Rk}G$  is the temperature dependent change of Gibb's free energy of the reaction and the product is a conversion factor from partial pressures and coverages to concentrations. This equation can be used to determine the rate coefficients of the reverse reactions. However, at time of mechanism development, the thermodynamic potentials of the surface species are usually unknown.

$$\Delta_{Rk}G(T) = \sum_{i=1}^{N_g} v_{ik} G_i(T) + \sum_{i=N_g+1}^{N_g+N_s} v_{ik} G_i(T) \quad (17)$$

known                      unknown

Nevertheless, since a surface reaction mechanism typically contains more pairs of reversible surface reactions than surface species, the reaction rate coefficients cannot be chosen independently. During development of the reaction mechanism, we have to apply an adjustment procedure to ensure that for a proposed set of rate coefficients thermodynamic functions  $G_i(T)$  exist for all surface species.

We have improved the method described in [24] to also ensure that the functions  $G_i(T)$  behave in a thermodynamic meaningful way, i.e., that the resulting heat capacity is always positive. Under these circumstances, we can approximate  $x_{f/rk}(T) = \ln k_{f/rk}(T)$  and  $y_i(T) = G_i(T)/RT$  by functions of the form  $a + b \ln T + c/T$ . Then Eq. (16) becomes

$$x_{fk}(T) - x_{rk}(T) = \ln \left( \prod_{i=1}^{N_g+N_s} c_{i,0}^{v_{ik}} \right) - \sum_{i=1}^{N_g} v_{ik} \frac{G_i(T)}{RT} - \sum_{i=N_g+1}^{N_g+N_s} v_{ik} y_i(T) \quad (18)$$

The aim of the adjustment algorithm is to find minimum (weighted) changes for the functions  $x_{f/rk}(T)$  such that functions

**Table 4**

Proposed microkinetic surface reaction mechanism for Pt catalyzed CO oxidation reaction.

Reaction	A [mol, cm, s]/S <sup>0</sup>	$\beta$	E <sub>a</sub> [kJ/mol]
O <sub>2</sub> + (Pt) → O <sub>2</sub> (Pt)	5.000 × 10 <sup>-2</sup>	0.000	0.00
O <sub>2</sub> (Pt) → O <sub>2</sub> + (Pt)	5.243 × 10 <sup>11</sup>	-0.069	19.573
O <sub>2</sub> (Pt) + (Pt) → O(Pt) + O(Pt)	8.325 × 10 <sup>13</sup>	0.000	39.933
O(Pt) + O(Pt) → O <sub>2</sub> (Pt) + (Pt)	4.444 × 10 <sup>21</sup>	0.000	264.067
			-88.2 × ⊖ <sub>0</sub>
CO + (Pt) → CO(Pt)	8.400 × 10 <sup>-1</sup>	0.000	0.000
CO(Pt) → CO + (Pt)	7.635 × 10 <sup>12</sup>	-0.139	143.145
			-29.3 × ⊖ <sub>0</sub>
CO <sub>2</sub> + (Pt) → CO <sub>2</sub> (Pt)	3.193 × 10 <sup>-3</sup>	-0.035	2.686
CO <sub>2</sub> (Pt) → CO <sub>2</sub> + (Pt)	1.894 × 10 <sup>10</sup>	0.139	21.855
CO(Pt) + O <sub>2</sub> (Pt) → CO <sub>2</sub> (Pt) + O(Pt)	4.124 × 10 <sup>13</sup>	0.069	9.494
			+44.1 × ⊖ <sub>0</sub>
CO <sub>2</sub> (Pt) + O(Pt) → CO(Pt) + O <sub>2</sub> (Pt)	2.910 × 10 <sup>23</sup>	-0.069	272.506
			+29.3 × ⊖ <sub>0</sub>
CO(Pt) + O(Pt) → CO <sub>2</sub> (Pt) + (Pt)	4.764 × 10 <sup>13</sup>	0.069	101.361
			-29.3 × ⊖ <sub>0</sub>
CO <sub>2</sub> (Pt) + (Pt) → CO(Pt) + O(Pt)	6.297 × 10 <sup>20</sup>	-0.069	140.239
			+44.1 × ⊖ <sub>0</sub>

$y_i(T)$  exist for all surface species. Thus, the algorithm not only yields a set of thermodynamic consistent rate coefficients, but also suitable thermodynamic potentials for the surface species.

### 3.4. Surface reaction mechanism

A refined microkinetic reaction mechanism was developed for numerical simulation of the CO oxidation reaction over Pt/Al<sub>2</sub>O<sub>3</sub> (Table 4). It consists of two possible routes according to the Langmuir–Hinshelwood mechanism, one representing the broadly accepted CO oxidation reaction pathway on a platinum surface, the other based on the reaction scheme proposed by Allian et al. [25]. The reaction mechanism involves elementary steps for molecular CO, CO<sub>2</sub>, and O<sub>2</sub> absorption on Pt, dissociation of molecularly adsorbed O<sub>2</sub>(Pt), reactions between the surface species CO(Pt) and O(Pt), respectively CO(Pt) and O<sub>2</sub>(Pt), and desorption of CO(Pt), O<sub>2</sub>(Pt) and CO<sub>2</sub>(Pt) into the gas phase. Each elementary reaction step is considered as reversible. Common microkinetic reaction mechanisms exclusively regard the reaction of adsorbed CO(Pt) with adsorbed O(Pt) for CO<sub>2</sub>-formation, assuming that dissociation of O<sub>2</sub>(Pt) occurs much faster than the surface reactions [26–28]. However, recent kinetic analysis of the platinum catalyzed CO oxidation reaction by Allian et al. resulted in kinetic orders of about 1 and -1 for O<sub>2</sub> and CO, respectively [25]. This observation is inconsistent with the assumption of quasi-equilibrated dissociative adsorption of O<sub>2</sub>, which would give rise to a reaction order of 0.5 for O<sub>2</sub>. Furthermore, Harold and Garske demonstrated that the commonly used three-step Langmuir–Hinshelwood mechanism fails in predicting several basic kinetic trends, such as the correct CO reaction order in the low and high CO pressure regimes [29]. After analyzing various kinetic models, they concluded that the limitations of the broadly accepted reaction mechanism can be overcome by including Eley–Rideal type reactions and steps involving molecular oxygen. Therefore, we now present a surface reaction mechanism which also takes the direct reaction of CO(Pt) with molecularly adsorbed O<sub>2</sub>(Pt) into account, which is kinetically equivalent to the formation of a O(Pt)=O–C(Pt)=O transition state via reaction of O<sub>2</sub> from the gas phase with (Pt)–CO(Pt) site pairs, as proposed by Allian et al. [25].

The starting points for the kinetic parameters of the model were taken from literature. Values for the sticking coefficient, pre-exponential factors and activation energies for oxygen adsorption, desorption, dissociation, and association are based on values published by Kissel–Osterrieder et al. [30] and Elg et al. [31]. Kinetic parameters used for CO adsorption and desorption, as well as for

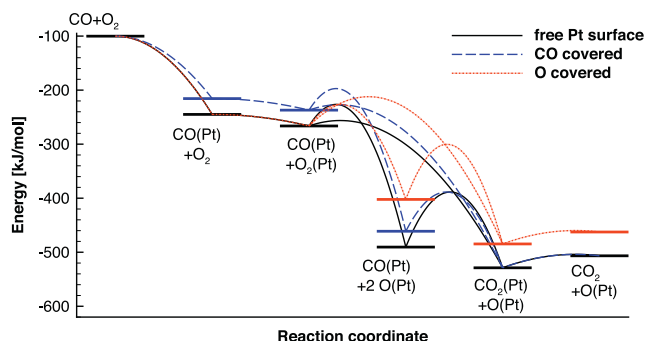


Fig. 3. Potential energy diagram for the elementary steps of the reaction mechanism for Pt catalyzed CO oxidation.

CO<sub>2</sub> desorption and the surface reaction of adsorbed CO(Pt) with O(Pt), are derived from a publication of Koop et al. [26]. Model parameters for CO<sub>2</sub> adsorption, CO<sub>2</sub>(Pt) dissociation, and coverage dependencies of the activation barriers for the elementary reaction steps are based on previous works of Kahle [32]. The value for the activation energy of CO<sub>2</sub> formation via reaction of CO(Pt) with molecularly adsorbed oxygen O<sub>2</sub>(Pt) is related to the activation barrier for the formation of the O(Pt)=O–C(Pt)=O transition state, calculated from DFT by Allian et al. [25].

In order to concentrate on the CO oxidation reaction and for simplicity, no reactions with water species are included. However, when comparing simulation results presented in this paper with calculations including elementary reaction steps with water species, published by Koop et al. [26], we observed that the effect of water can be neglected in our case.

The potential energy diagram for the elementary steps of the surface reaction mechanism is depicted in Fig. 3. It is clearly shown that the activation energies of the two possible reaction paths strongly depend on the surface coverage. For O(Pt) covered platinum surface, the activation energy is lower for the broadly accepted CO<sub>2</sub>-formation mechanism. However, for CO covered and free platinum surfaces, direct reaction of CO(Pt) with O<sub>2</sub>(Pt) is more favorable from the kinetic point of view. Since there is a broad agreement that CO oxidation at low temperatures occurs on a platinum surface which is nearly saturated with CO, it is crucial to take this reaction path into account [3].

## 4. Results and discussion

The platinum dispersion and the CO light-off temperature were experimentally determined for a commercial Pt/Al<sub>2</sub>O<sub>3</sub> DOC in a fresh state and subsequent to various catalyst aging treatments. Furthermore, a refined microkinetic model for the platinum catalyzed oxidation of CO, comprising two different paths for CO<sub>2</sub> formation, is developed and used for simulation of the CO light-off experiments. The results are discussed in the following.

### 4.1. Aging correlation

The average platinum dispersion of the fresh catalyst samples determined by CO-TPD was 9%. The average inlet temperature at which 50% CO was oxidized during light-off measurements was 444 K for the fresh samples; the temperature measured at the catalyst outlet was 458 K in average. In the following, it is referred to the outlet temperature as it corresponds to the prevalent temperature inside the catalyst. However, the found correlations equally count for the inlet temperature.

The evolution of platinum dispersion and CO light-off temperature with aging time and aging temperature for lean aging atmospheres is shown in Figs. 4 and 5, respectively. Since the samples exhibited slightly different activities, for a better comparison, the depicted platinum dispersion is scaled to the dispersion of the particular fresh sample. Also, the change of light-off temperature is related to the respective fresh sample.

Normalization of the dispersion:

$$D(\text{norm.}) = \frac{D(x)}{D(0)} \quad (19)$$

Change of CO light-off temperature:

$$\Delta T_{50} = T_{50}(T) - T_{50}(0) \quad (20)$$

According to expectations, the platinum dispersion decreases with increasing degree of catalyst aging and a shift to higher temperatures is observed for the light-off of the CO oxidation reaction. The experimental results show that the change of the catalytic surface area as well as the CO light-off temperature, and therefore the catalytic activity, is most significant in the first hours of aging. Furthermore, a higher aging temperature leads to accelerated catalyst deactivation and an earlier onset of the leveling-off behavior.

Similar trends have been observed for all investigated lean aging atmospheres. It was found that the increase of the CO light-off

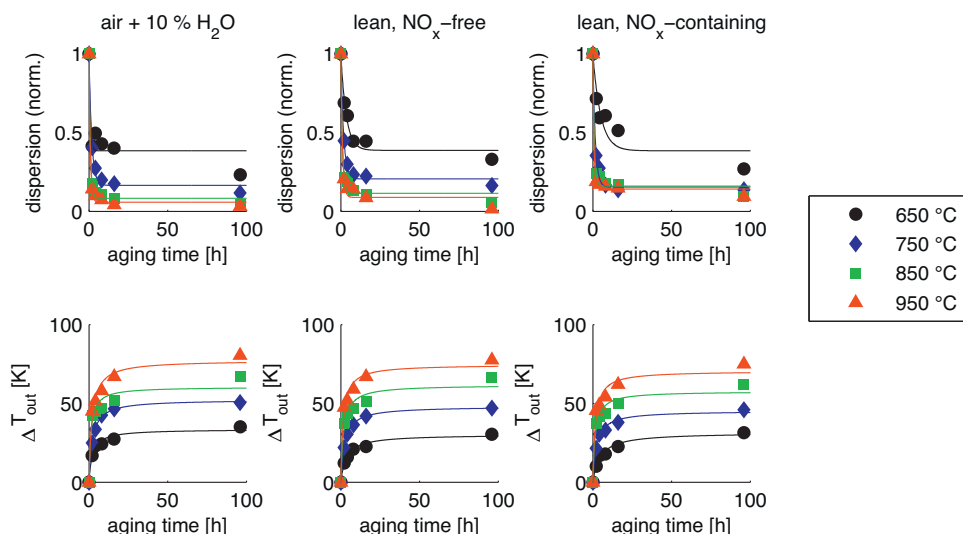


Fig. 4. Normalized platinum dispersion and CO light-off temperature increase as a function of aging time.

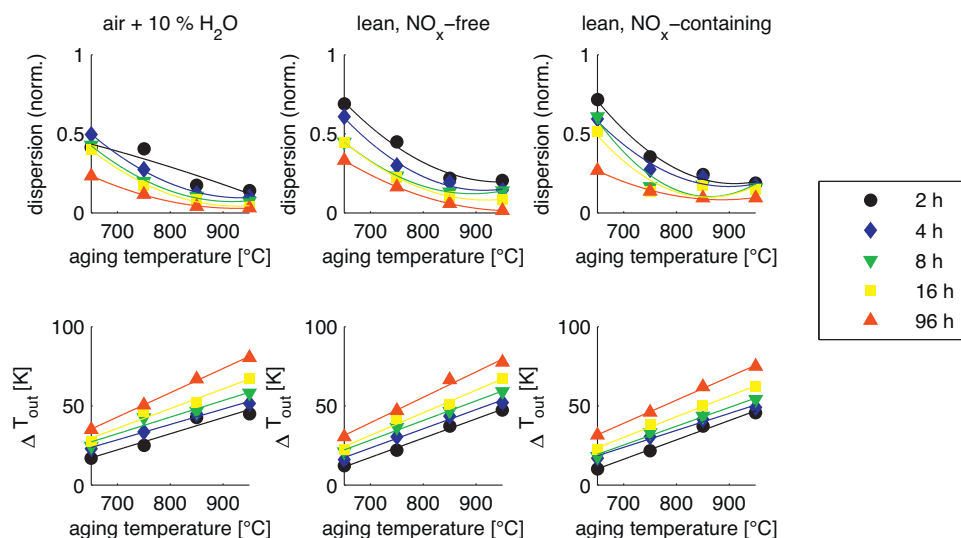


Fig. 5. Platinum dispersion and CO light-off temperature increase as a function of aging temperature.

temperature with aging time can be described by a rational correlation function while the noble metal dispersion decreases exponentially with aging time. The change of dispersion with aging temperature can be reproduced by a quadratic polynomial function. Furthermore, a linear increase in the CO light-off temperature with aging temperature has been observed, indicating a linear reduction of the overall activity of the catalyst. It can be seen from Fig. 5 that the influence of the aging temperature on the catalytic activity rises for very long aging times. The incline of CO light-off temperature with aging temperature is steeper for 96 h of aging treatment compared to a shorter aging duration.

Slight differences in aging behavior were found depending on the exact composition of the aging atmosphere. The experimental results show that platinum particle sintering is most pronounced for samples aged in air + 10 vol.% H<sub>2</sub>O, followed by aging in lean NO<sub>x</sub>-free model exhaust gas, whereas the presence of NO<sub>x</sub> seems to inhibit particle growth. The same order was observed for the change of CO light-off temperature. Thus, the severity of catalyst aging depending on the aging atmosphere can be summarized as follows: air + 10 vol.% H<sub>2</sub>O > lean NO<sub>x</sub>-free model exhaust gas > lean NO<sub>x</sub>-containing model exhaust gas.

For all investigated lean aging atmospheres, a clear correlation between the catalytic activity and the catalytic active surface area has been observed (Fig. 6). Independent of the aging temperature, aging time and the exact composition of the lean aging atmosphere, it exhibits the same trend and can be described by an exponential function. There are only minor distinctions between the different oxygen-rich aging atmospheres concerning the exact correlation between activity and catalytic surface area, especially in the severe aging region. Although the dispersion remains relatively high after

aging in lean NO<sub>x</sub>-containing model exhaust gas, the extent of the temperature increase for the light-off of the CO oxidation reaction is comparable to the activity decrease caused by aging treatment in air + 10 vol.% water.

However, aging treatment in N<sub>2</sub> leads to a strikingly different behavior. In this case, the impact of aging on the noble metal dispersion and the catalytic activity is less pronounced. Furthermore, in spite of a notable decrease of the platinum dispersion, the activity of the catalyst is scarcely affected and no distinct correlation between these two parameters can be perceived. Therefore, it is supposed that the mechanism of noble metal sintering depends on the oxygen content of the aging atmosphere: with an oxygen-poor environment leading to a particle size distribution more beneficial to the catalyst activity than the particle sizes arising from lean aging conditions. This assumption is discussed in detail in the following section.

#### 4.2. Structure sensitivity and sintering mechanism

Although the platinum dispersion decreased to 40% of the original value after 16 h aging at 850 °C in N<sub>2</sub>, the CO light-off temperature surprisingly remained the same as for the fresh catalyst sample. In contrary, a sample aged for 4 h at 750 °C in lean NO<sub>x</sub>-free model exhaust gas yielded a similar platinum dispersion, but a concomitant rise of the CO light-off temperature of 30 K was observed.

The TPD spectra of both aged catalyst samples and a fresh sample following CO chemisorption are shown in Fig. 7. The fresh catalyst exhibits a very broad temperature range in which desorption occurs, indicating the presence of a huge variety of desorption sites with different CO adsorption energies. Determination of distinct adsorption sites is not possible due to overlapping of desorption peaks. A closer examination of the TPD spectra reveal significant differences in the CO desorption behavior of the aged samples in spite of a similar over-all dispersion. For the sample aged for 4 h at 750 °C in lean NO<sub>x</sub>-free model exhaust, the desorption features above 600 K disappeared. The desorption range of the sample aged for 16 h at 850 °C in N<sub>2</sub> is even narrower with the peak temperature at 380 K than for the fresh and lean aged samples, and desorption already starts at a lower temperature. The low desorption temperature indicates that CO is weakly bound on the catalyst aged in N<sub>2</sub>.

In previous studies, desorption features with peak temperatures at around 400 K had been assigned to CO desorption from terrace

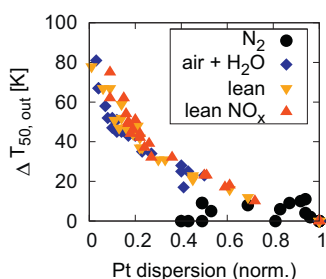
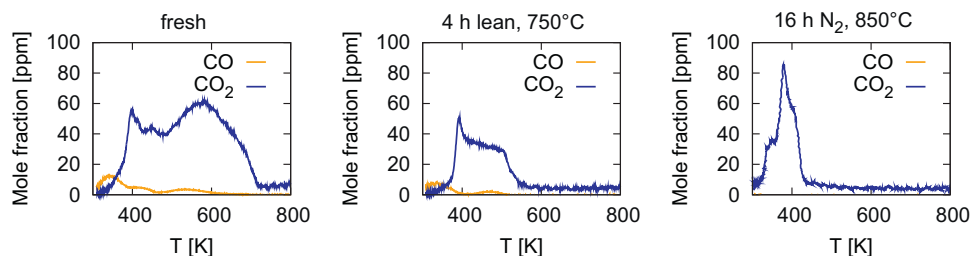


Fig. 6. Correlation between CO light-off temperature increase and platinum dispersion for all investigated aging atmospheres.



**Fig. 7.** TPD spectra of a fresh catalyst sample with 9.1% Pt dispersion (left), a sample aged in lean atmosphere for 4 h at 750 °C with 3.2% Pt dispersion (center), and a sample aged in N<sub>2</sub> for 16 h at 850 °C with 3.3% Pt dispersion (right).

sites since they were dominant on high index planes and large Pt particles while high temperature desorption features emerged for small platinum particles and were ascribed to desorption from step sites [33–36]. Therefore, it is supposed that aging in N<sub>2</sub> induces a different particle sintering mechanism compared to aging under lean conditions, leading to a distinct particle size distribution which is more beneficial to CO oxidation. Indeed, structure sensitivity for CO oxidation has been observed before in several studies [3]. Szabo et al. [34] reported that CO oxidation preferentially occurred on the terrace sites of a stepped Pt(112) surface and suggested that the elementary step producing CO<sub>2</sub> from adsorbed CO and oxygen is structure sensitive, with a smaller activation energy on terrace sites. Zafirios and Gorte studied CO oxidation on Pt/ $\alpha$ -Al<sub>2</sub>O<sub>3</sub>(0001). They observed considerably higher turnover frequencies and a lower activation energy for CO oxidation on 14 nm platinum particles than on 1.7 nm particles [36]. The authors suggested that the observed structure sensitivity could be explained by changes in the desorption kinetics of CO with particle size. Because low temperature desorption features around 400 K only have been observed at high CO coverage for all but the smallest platinum particles, they are supposed to be the result of repulsive adsorbate–adsorbate interactions. The radius of curvature of small particles is assumed to be small enough to reduce repulsive interactions. In contrary, the data published by Berlowitz et al. [37] indicate structure insensitive kinetics. However, their findings are based on the comparison of specific reaction rates for a Pt(100) single crystal and a supported Pt/SiO<sub>2</sub> catalysts containing 5% Pt. It is well known that the Pt(100) surface is prone to adsorbate induced reconstructions [38]. Therefore, the excess of CO used in their experiments ( $p_{\text{CO}}:p_{\text{O}_2} = 2:1$ ) might cause surface reconstructions in a way that both investigated catalyst types become comparable. Furthermore, high CO partial pressures lead to a prevalence of weakly adsorbed CO species and repulsive adsorbate–adsorbate interactions, neutralizing the effect of different adsorption sites.

Our experimental results are in excellent agreement with the observations of Zafirios and Gorte [36]. The significant downshift of the desorption maximum for CO TPD on the sample aged in N<sub>2</sub> indicates an increase of platinum particle size in a manner which compensates the loss of dispersion by an increase of turnover rate for CO oxidation. Whereas small platinum particles exist on the fresh and the lean aged sample, contributing to a relatively high dispersion but small reaction rates due to poisoning of the platinum surface by strongly adsorbed CO.

It can be ruled out that the unexpected behavior of the samples aged in N<sub>2</sub> emerged from an error of dispersion measurement due to a possible change of CO adsorption stoichiometry in consequence of aging treatment. Assuming that the platinum dispersion is not affected by aging according to the unchanged CO light-off temperature, the CO:metal adsorption stoichiometry changes from 1:1 for the fresh sample to a stoichiometry between 1:2 and 1:3 for the aged catalyst, which means that the type of adsorbed CO changes from linear to bridged and capped or dissociative adsorption. However, the higher adsorption energy of bridged and capped

CO surface species compared to linear adsorbed CO would be in disagreement with the decreased average desorption temperature after aging.

Furthermore, washcoat effects can be considered as negligible since it has been shown previously that CO desorption does not depend on the structure of the Al<sub>2</sub>O<sub>3</sub> support [33].

Our experimental results indicate that the particle sintering mechanism depends on the oxygen concentration of the aging atmosphere. The sintering mechanism of platinum nanoparticles on an amorphous Al<sub>2</sub>O<sub>3</sub> support was previously studied under lean conditions by means of in situ transmission electron microscopy [39]. Simonsen et al. reported that the sintering of platinum particles was mediated by an Ostwald ripening process with migration of particular platinum atoms. Due to the differing particle size distribution arising from aging in N<sub>2</sub>, it is assumed that aging in an oxygen-free atmosphere induces a different platinum sintering mechanism compared to aging in an oxygen-containing atmosphere. It is suggested that particle growth in this case occurs via particle migration. Hereby, very small platinum particles combine to larger particles giving rise to a decreased noble metal dispersion but an increased turnover frequency for CO oxidation. Thus, the CO light-off temperature remains unchanged although the catalytic surface area decreases.

#### 4.3. Simulation results

Due to the clear correlation between catalytic activity and catalytic surface area for lean aging atmospheres, one single elementary-step based model (Table 4) was used for the simulation of the CO light-off experiments. In order to account for the light-off temperature shift caused by thermal aging, the model parameter  $F_{\text{cat}/\text{geo}}$  was scaled according to the measured platinum dispersion.

The simulation results for the CO light-off experiments are depicted in Fig. 8. It is clearly recognizable that the proposed model describes the experimental results very well within the measurement accuracy for the platinum dispersion. It is important to note that no kinetic model parameters have to be adjusted for the simulation of the behavior of differently aged catalysts regarding the CO oxidation reaction. Solely the catalytic surface area has been adapted to the experimentally determined platinum dispersion.

The correlation between CO light-off temperature and platinum dispersion from experiment and simulation is depicted in Fig. 9. It is clearly shown that the model is able to describe the coherence of the two variables correctly. As a conclusion, the experimentally found correlation between catalytic activity and catalytically active surface area is successfully used for the simulation of the activity change caused by thermal aging.

As shown in Fig. 10, it is obvious from reaction flow analysis that the respective contribution of the two different reaction paths for CO<sub>2</sub> formation strongly depend on the value of the model parameter  $F_{\text{cat}/\text{geo}}$  and therefore, on the platinum dispersion. In case of low platinum dispersion, CO<sub>2</sub> is mainly formed by direct reaction of CO(Pt) with molecularly adsorbed O<sub>2</sub>(Pt), whereas CO<sub>2</sub>



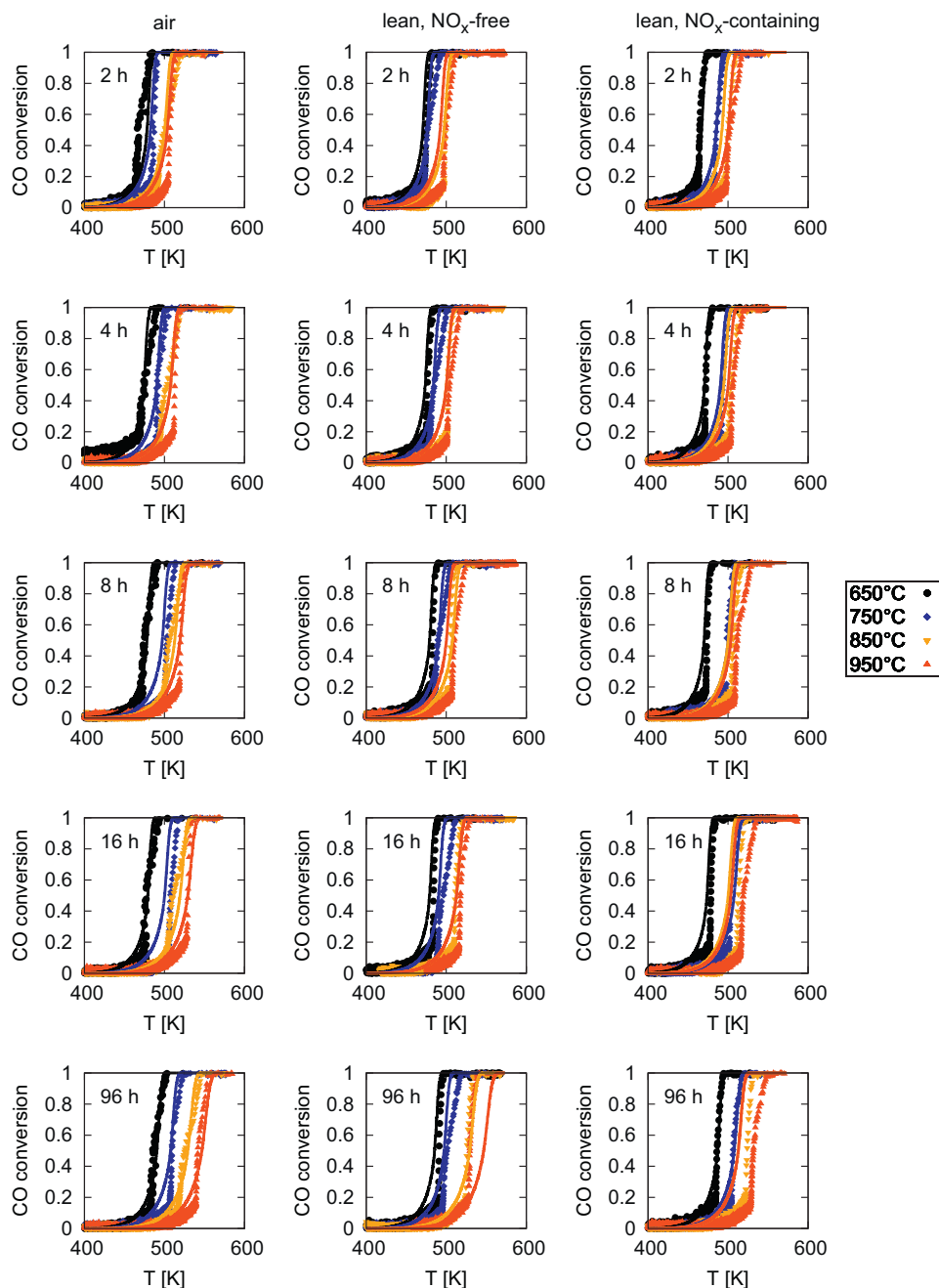


**Fig. 8.** Simulation (lines) of CO light-off experiments (symbols). Aging effects are regarded by changing the model parameter  $F_{\text{cat}/\text{geo}}$  according to the measured platinum dispersion.

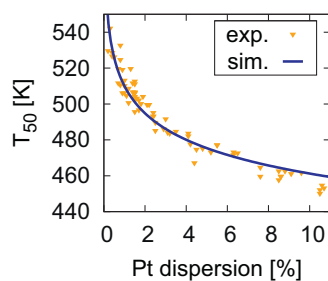


**Fig. 9.** Correlation between CO light-off temperature and platinum dispersion: comparison of simulation and experiment.

formation from reaction of CO(Pt) with atomic O(Pt) gets more important for higher platinum dispersions, as the rate of oxygen dissociation increases with the catalytic surface area. The simulated CO light-off temperatures for the depicted cases  $F_{\text{cat}/\text{geo}}$  1, 13 and 42 are 547 K, 487 K, and 463 K, respectively.

The simulated evolution of the surface coverage during CO light-off measurements is shown exemplarily for  $F_{\text{cat}/\text{geo}}$  13 in Fig. 11. Before onset of the CO oxidation reaction, the platinum surface is almost completely covered by CO(Pt). In agreement with the experimental observation of Salomons et al. [40], the reaction starts at the end of the catalyst and then the reaction front propagates backwards toward the reactor entrance. After ignition of the reaction, the surface concentration of CO(Pt) at the rear of the catalyst falls to zero, whereas the concentration of O(Pt) increases to the same extent. The higher the temperature, the more the platinum surface

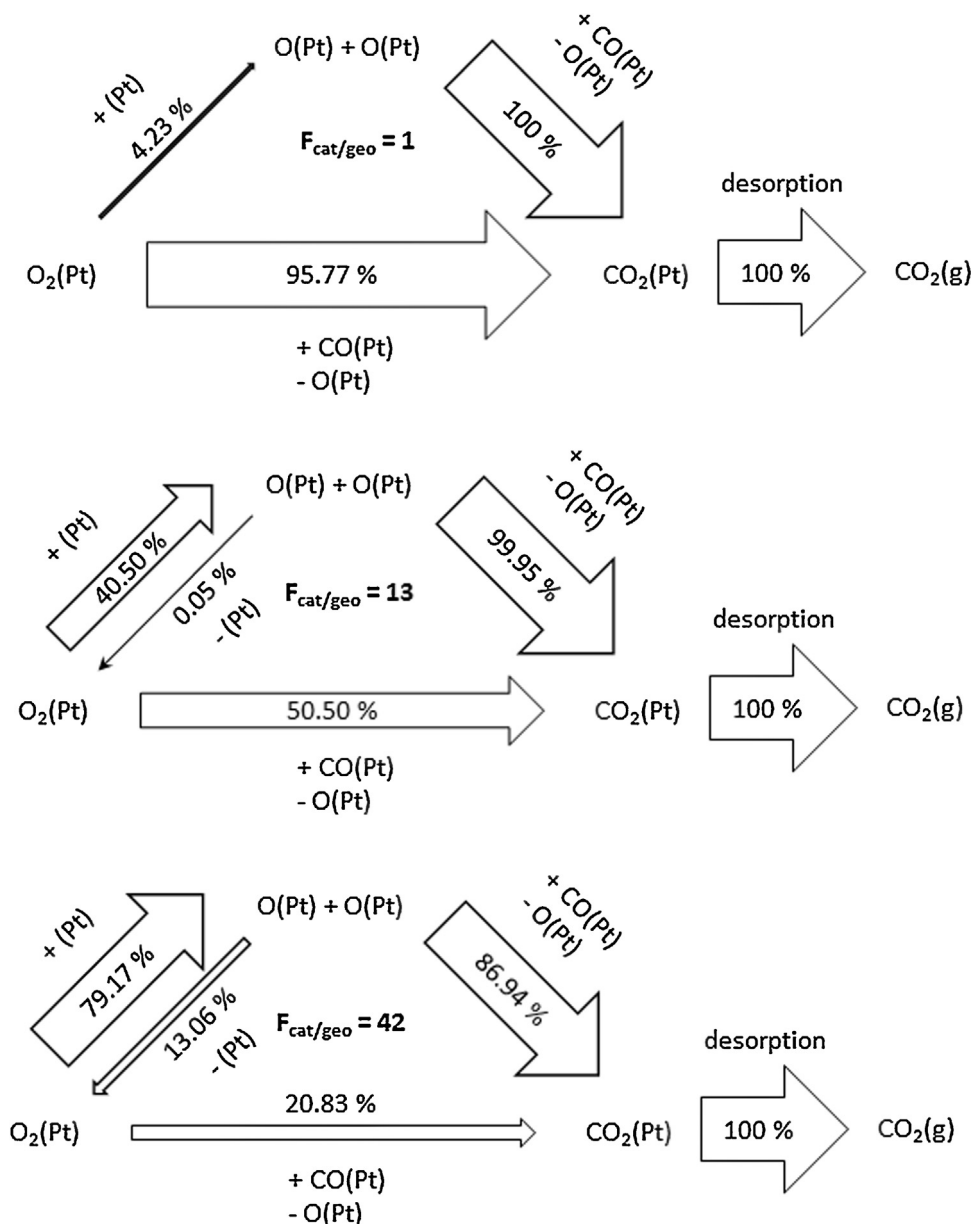


Fig. 10. Reaction flow analysis at  $T_{50}$ : comparison of different  $F_{cat/geo}$  values.

is covered by atomically adsorbed oxygen species  $O(Pt)$  instead of  $CO(Pt)$ . For sufficiently high temperatures, CO oxidation is already completed at the catalyst entrance. It is noteworthy that there is a remarkable amount of free Pt sites at each stage of the reaction. The location of the reaction front is the same as for the free Pt sites. Further, small fractions of the platinum surface at the reaction front are covered by  $CO_2(Pt)$  and molecularly adsorbed oxygen species  $O_2(Pt)$ . Note that there are two peaks at different axial locations for the surface concentration of  $CO_2(Pt)$ . The peak downstream represents  $CO_2$  formation from reaction of  $CO(Pt)$  with molecularly adsorbed oxygen  $O_2(Pt)$ , whereas the peak further upstream originates from reaction of  $CO(Pt)$  with  $O(Pt)$ .

#### 4.4. Mass transfer limitation

In Fig. 12, the measured and simulated axial concentration profiles of CO and  $CO_2$  are shown. The experiment has been performed with the catalyst sample aged for 96 h at 650 °C in lean  $NO_x$ -containing model exhaust gas. The  $F_{cat/geo}$  value of

13 used for simulation was calculated from the experimentally determined dispersion. As boundary condition for modeling with DETCHEM<sup>CHANNEL</sup> we applied the measured wall temperature profile, which is also consistent with nearly adiabatic conditions. The inlet gas velocity was 0.76 m/s at 508 K. Mass transfer limitation by pore diffusion within the washcoat is taken into account by using the effectiveness factor approach and a detailed reaction-diffusion model, respectively. In this case, the effectiveness factor model overestimates the diffusion limitations, which leads to deferred light-off profiles. The effectiveness factor model is based on the assumption that the representative species is consumed by a first order reaction. However, in the case of platinum catalyzed CO oxidation negative effective reaction orders occur beyond a critical CO concentration [25]. This leads to an increase of the effective reaction rate with decreasing CO concentration, i.e. the effectiveness factor is actually greater than one, which cannot be captured by the simple effectiveness factor model based on Thiele modulus.

Considering internal mass transport limitations by a reaction-diffusion model resulted in excellent agreement between

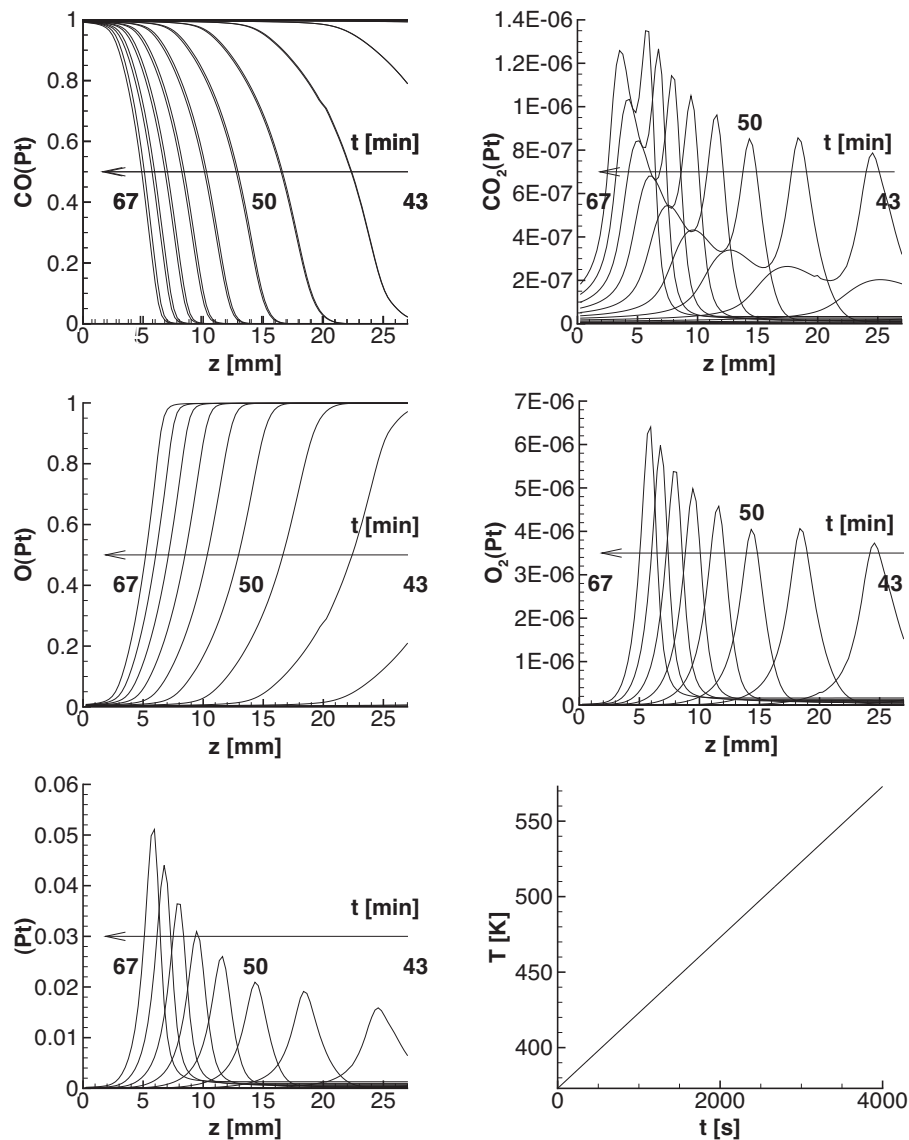


**Fig. 11.** Simulated evolution of surface coverage during CO light-off experiment for  $F_{\text{cat/geo}}$  13 (373–573 K, 3 K/min). Gas inlet: 1 vol.% CO, 7 vol.% CO<sub>2</sub>, 12 vol.% O<sub>2</sub>, 10 vol.% H<sub>2</sub>O, N<sub>2</sub> balance.

simulated and measured values. The slight axial shift of the simulated concentration profiles downstream relative to the experimental profiles is comprehensible when regarding the impact of the capillary on the flow field. Hettel et al. [41] have shown by means of CFD simulations that the residence time at the probe tip is generally larger as compared to the equivalent axial

position of an empty channel. This leads to an apparently further reaction progress and an axial shift of the measured concentration profiles upstream. Thus, in case of an empty channel, the actual concentration profiles would be shifted downstream relative to

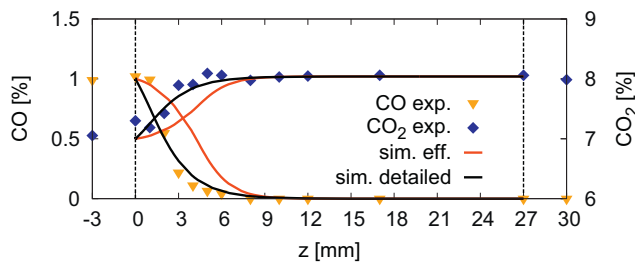


**Fig. 12.** Measured (symbols) and simulated (lines) axial concentration profiles during CO oxidation at 508 K,  $F_{\text{cat/geo}}$  13. Comparison of detailed diffusion model and effectiveness factor model. Gas inlet: 1 vol.% CO, 7 vol.% CO<sub>2</sub>, 12 vol.% O<sub>2</sub>, 10 vol.% H<sub>2</sub>O, N<sub>2</sub> balance.

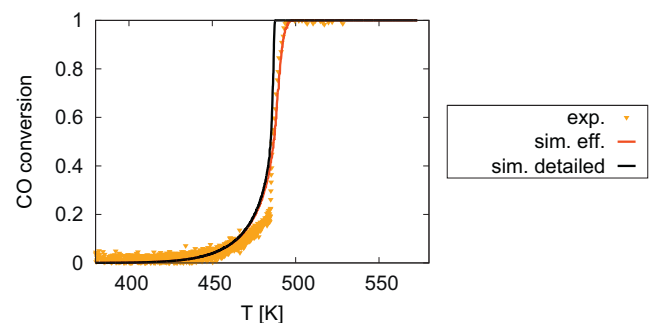


**Fig. 13.** Simulation (lines) of the CO light-off experiment (symbols) for the catalyst sample aged for 96 h at 650 °C in lean NO<sub>x</sub>-containing model exhaust gas,  $F_{\text{cat/geo}}$  13: Comparison of reaction-diffusion washcoat model and effectiveness factor approach.

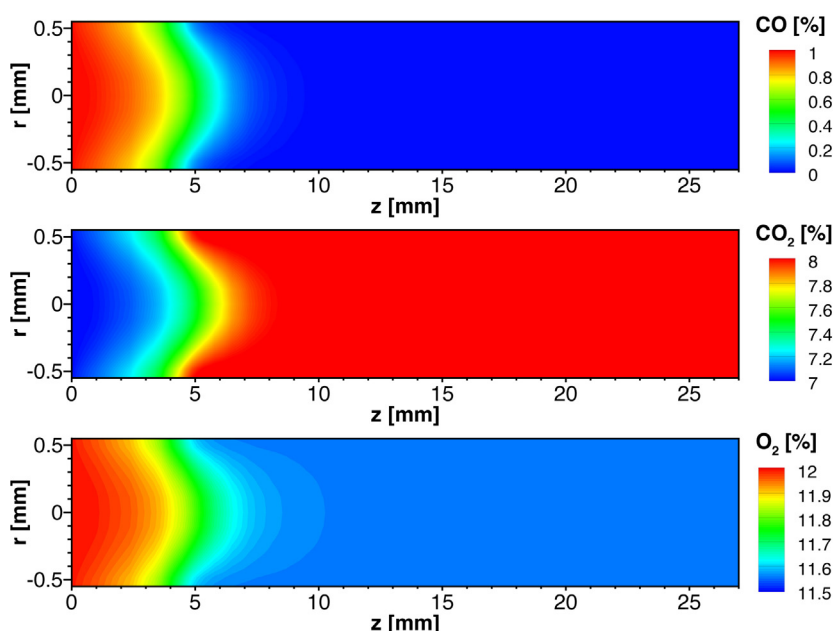


**Fig. 14.** Simulated gas phase concentration profiles of CO, CO<sub>2</sub> and O<sub>2</sub> inside a channel for CO oxidation at 508 K,  $F_{\text{cat/geo}}$  13, detailed reaction-diffusion model.  $z$ : axial coordinate,  $z=0$ : catalyst entrance;  $r$ : radius,  $r=0$ : centerline.

the experimentally determined profiles and therefore in better agreement with the simulated profiles. However, for a quantitative correction of the experimental data, a three-dimensional CFD calculation would be necessary and the position of the probe in the cross-sectional plane has to be clearly defined, which is far beyond the scope of this paper.

In Fig. 13, the simulation results for the CO light-off which arise from regarding internal mass transfer limitation by using the effectiveness factor approach are compared with the data obtained from calculation with a reaction-diffusion washcoat model. Despite the differences discussed above, it can be seen that both models yield comparable results. For low CO concentration, i.e. near full conversion, the assumption of a first order reaction is fulfilled, whereas at high CO concentrations, the reaction rate is kinetically limited and the effectiveness factor becomes unity. Only for intermediate CO concentrations, the differences between the two models can be observed. However, this only affects the simulation results beyond light-off. Therefore, the time saving effectiveness factor approach is applicable for simulation of CO light-off experiments.

The contour plots of the simulated gas phase species profiles are shown in Fig. 14. It is clearly recognizable that there are moderate radial concentration gradients. Thus, the exact location of the suction probe in the  $xy$ -plane is another possible source of uncertainty for the experimentally determined concentration profiles.

However, for simulation of CO light-off experiments, the effect of mass transfer limitation by radial diffusion in bulk flow can be neglected as there is a steep concentration change around the light-off point due to the highly exothermic CO oxidation reaction. Therefore, simulation of the CO light-off experiments by using a CSTR cascade model as a simple, fully transient 1 D reactor model provides sufficiently accurate results.

## 5. Conclusion and outlook

The platinum dispersion and the catalytic activity of a commercial Pt/Al<sub>2</sub>O<sub>3</sub> DOC were determined subsequent to various aging treatments. Thereby, aging temperature and aging time, as well as the aging atmosphere were varied.

Similar trends are observed for all investigated lean aging atmospheres:

- Catalytic surface area and catalytic activity decrease with increasing degree of catalyst aging.
- Most significant changes in the first hours of aging.
- Higher aging temperature leads to accelerated catalyst deactivation and an earlier onset of the leveling-off behavior.
- Impact of aging temperature on catalytic activity is increased for very long aging times.
- Clear correlation between catalytic activity and catalytic surface area.

However, aging treatment in N<sub>2</sub> leads to a significantly different behavior:

- In spite of a notable decrease of the Pt dispersion, the catalyst activity is scarcely affected.
- No distinct correlation between catalytic activity and catalytic surface area.

Since it is observed that aging in N<sub>2</sub> leads to a particle size distribution which is more beneficial to the catalyst activity, as compared to particle sizes arising from lean aging conditions, we suppose that the sintering mechanism for the platinum particles depend on the oxygen content of the aging atmosphere, with an Ostwald ripening process occurring in lean atmosphere and particle migration in N<sub>2</sub>. Furthermore, our observations imply that platinum catalyzed CO oxidation is structure-sensitive due to changes in CO desorption kinetics with platinum particle size, whereby terrace sites are most active.

Additionally, a refined microkinetic model for the platinum catalyzed oxidation of CO is developed which comprises two different paths for CO<sub>2</sub> formation. The experimentally found correlation between catalytic activity and catalytic active surface area is successfully used for the simulation of the activity change caused by lean hydrothermal aging.

Furthermore, a suction probe technique is used for the measurement of spatially resolved gas phase concentration profiles



of CO and CO<sub>2</sub> during CO oxidation at full conversion. The newly developed microkinetic model is also able to describe the axial concentration profiles correctly. However, for a quantitative comparison of the simulation results with the experimental data, a three-dimensional CFD calculation taking the influence of the probe on the flow field into account would be necessary, which is far beyond the scope of this paper.

It is shown that a successful correlation of reaction kinetics with characteristic variables of the catalyst substantially simplifies the recalibration of an existing model in the case of activity change. However, the presented strategy is not applicable as soon as structure sensitivity plays a role. In order to take structure sensitivity into account, future microkinetic models using the mean field approximation should not only regard coverage dependency of activation barriers, but also allow for changes of the activation energies due to structural changes of the catalyst surface. This is especially crucial if reversible alteration of the catalyst's state occurs in a short time scale and affects the reaction rate, e.g., adsorbate induced surface restructuring or change of the oxidation state, as it is the case for platinum catalyzed NO oxidation under conditions which are relevant for exhaust gas aftertreatment.

## Acknowledgements

We gratefully thank Forschungsvereinigung Verbrennungskraftmaschinen e.V. (FVV) for financial support, Umicore AG & Co. KG for providing the catalyst and our partners within the FVV project, K. Hauff and U. Nieken (ICVT, University of Stuttgart). Furthermore, the authors acknowledge A. Ünal for help during concentration profile measurements and L. Maier for sharing her longstanding experience with the development of microkinetic reaction mechanisms.

## References

- [1] O. Deutschmann, J.-D. Grunwaldt, *Chem. Ing. Tech.* 85 (2013) 595–617.
- [2] W.S. Epling, L.E. Campbell, A. Yezzerets, N.W. Currier, J.E. Parks, *Catal. Rev. Sci. Eng.* 46 (2004) 163–245.
- [3] A. Russell, W.S. Epling, *Catal. Rev.* 53 (2011) 337–423.
- [4] F.J.P. Schott, S. Steigert, S. Zuercher, M. Endisch, S. Kureti, *Chem. Eng. Process.: Process Intensification* 62 (2012) 54–58.
- [5] L. Lietti, P. Forzatti, I. Nova, E. Tronconi, *J. Catal.* 204 (2001) 175–191.
- [6] D. Bhatia, R.W. McCabe, M.P. Harold, V. Balakotaiah, *J. Catal.* 266 (2009) 106–119.
- [7] D. Chatterjee, V. Schmeißer, M. Frey, M. Weibel, in: O. Deutschmann (Ed.), *Modeling and Simulation of Heterogeneous Catalytic Reactions*, Wiley-VCH Verlag GmbH & Co. KGaA, Weinheim, 2011, pp. 303–343.
- [8] C. Brinkmeier, G. Eigenberger, J. Bernnat, U. Tuttli, V. Schmeißer, F. Opferkuch, *Chem. Ing. Tech.* 77 (2005) 1333–1355.
- [9] W. Boll, S. Tischer, O. Deutschmann, *Ind. Eng. Chem. Res.* 49 (2010) 10303–10310.
- [10] K. Hauff, U. Tuttli, G. Eigenberger, U. Nieken, *Appl. Catal. B: Environ.* 100 (2010) 10–18.
- [11] G. Bergeret, P. Gallezot, *Handbook of Heterogeneous Catalysis*, Wiley-VCH Verlag GmbH & Co. KGaA, Weinheim, 2008.
- [12] C. Karakaya, O. Deutschmann, *Appl. Catal. A: Gen.* 445 (2012) 221–230.
- [13] D. Livio, C. Diehm, A. Donazzi, A. Beretta, O. Deutschmann, *Appl. Catal. A: Gen.* 467 (2013) 530–541.
- [14] O. Deutschmann, S. Tischer, S. Kleditzsch, V.M. Janardhanan, C. Correa, D. Chatterjee, N. Mladenov, H.D. Mihn, H. Karadeniz, *DETCHEM Software package*, 2.4 ed, Karlsruhe, 2012, [www.detchem.com](http://www.detchem.com)
- [15] L.L. Raja, R.J. Kee, O. Deutschmann, J. Warnatz, L.D. Schmidt, *Catal. Today* 59 (2000) 47–60.
- [16] R.J. Kee, M.E. Coltrin, P. Glarborg, *Chemically reacting flow: theory and practice*, Wiley Interscience, Hoboken, NJ, 2003.
- [17] S. Tischer, C. Correa, O. Deutschmann, *Catal. Today* 69 (2001) 57–62.
- [18] H.S. Fogler, *Elements of Chemical Reaction Engineering*, 4th ed., Prentice Hall PTR, Upper Saddle River, NJ, 2006.
- [19] R.E. Hayes, A. Fadic, J. Mmbaga, H. Najafi, *Catal. Today* 188 (2012) 94–105.
- [20] R.E. Hayes, P.K. Mok, J. Mmbaga, M. Votsmeier, *Chem. Eng. Sci.* 62 (2007) 2209–2215.
- [21] H. Karadeniz, C. Karakaya, S. Tischer, O. Deutschmann, *Chem. Eng. Sci.* (2013), <http://dx.doi.org/10.1016/j.ces.2013.1009.1038>.
- [22] N. Mladenov, J. Koop, S. Tischer, O. Deutschmann, *Chem. Eng. Sci.* 65 (2010) 812–826.
- [23] L. Kunz, L. Maier, S. Tischer, O. Deutschmann, in: O. Deutschmann (Ed.), *Modeling and Simulation of Heterogeneous Catalytic Reactions*, Wiley-VCH Verlag GmbH & Co. KGaA, Weinheim, 2011, pp. 113–148.
- [24] L. Maier, B. Schadel, K.H. Delgado, S. Tischer, O. Deutschmann, *Top. Catal.* 54 (2011) 845–858.
- [25] A.D. Allian, K. Takanabe, K.L. Fudjula, X. Hao, T.J. Truex, J. Cai, C. Buda, M. Neurock, E. Iglesia, *J. Am. Chem. Soc.* 133 (2011) 4498–4517.
- [26] J. Koop, O. Deutschmann, *Appl. Catal. B: Environ.* 91 (2009) 47–58.
- [27] D. Chatterjee, O. Deutschmann, J. Warnatz, *Faraday Discuss.* 119 (2001) 371–384.
- [28] S. Salomons, M. Votsmeier, R.E. Hayes, A. Drochner, H. Vogel, J. Gieshoff, *Catal. Today* 117 (2006) 491–497.
- [29] M.P. Harold, M.E. Garske, *J. Catal.* 127 (1991) 524–552.
- [30] R. Kissel-Osterrieder, F. Behrendt, J. Warnatz, U. Metka, H.R. Volpp, J. Wolfrum, *Proc. Combust. Inst.* 28 (2000) 1341–1348.
- [31] A.-P. Elg, F. Eisert, A. Rosén, *Surf. Sci.* 382 (1997) 57–66.
- [32] L. Kahle, *Reaktionskinetik der Oxidation und Reformierung von H<sub>2</sub>, CO und CH<sub>4</sub> über Platinkatalysatoren*, Fakultät für Chemie und Biowissenschaften, Karlsruher Institut für Technologie, Karlsruhe, 2013.
- [33] E.I. Altman, R.J. Gorte, *J. Catal.* 110 (1988) 191–196.
- [34] A. Szabo, M.A. Henderson, J.T. Yates, *J. Chem. Phys.* 96 (1992) 6191–6202.
- [35] G.S. Zafiris, R.J. Gorte, *Surf. Sci.* 276 (1992) 86–94.
- [36] G.S. Zafiris, R.J. Gorte, *J. Catal.* 140 (1993) 418–423.
- [37] P.J. Berlowitz, C.H.F. Peden, D.W. Goodman, *J. Phys. Chem.* 92 (1988) 5213–5221.
- [38] R.W. McCabe, L.D. Schmidt, *Surf. Sci.* 66 (1977) 101–124.
- [39] S.B. Simonsen, I. Chorkendorff, S. Dahl, M. Skoglundh, J. Sehested, S. Helveg, *J. Am. Chem. Soc.* 132 (2010) 7968–7975.
- [40] S. Salomons, R.E. Hayes, M. Votsmeier, A. Drochner, H. Vogel, S. Malmberg, J. Gieshoff, *Appl. Catal. B: Environ.* 70 (2007) 305–313.
- [41] M. Hettel, C. Diehm, B. Torkashvand, O. Deutschmann, *Catal. Today* 216 (2013) 2–10.